$$w_{F1} = \frac{(1 - hs)^{(i_m + i_r)}}{(1 - s)^{i_r}},$$

$$w_{B(1)} = (1 - \tfrac{1}{2}hs)^{i_m}\left[\frac{2 - s - hs}{2(1 - s)}\right]^{i_r}$$

and that the fitnesses of later backcrosses converge geometrically on 1 at a rate of 1/2 per sexual generation (year). Using parameter values suggested for *Daphnia* (*46*) (s = 0.14 and h = 0.3) and setting $i_m = i_r = 55$ to give an F_1 fitness similar to what we observed, we obtain $m^*(2) = 35.7m$, $m^*(3) = 234m$, and $m^*(\infty) = 6703m$. Lower values of m^*, but still substantially greater than 1, can be obtained when i_m and i_r have more modest values. Thus, hybrid vigor can make gene flow many times stronger than would be predicted from the nominal migration rate under these conditions.

41. P. Pamilo, S. Pálsson, O. Savolainen, *Hereditas* **130**, 257 (1999).
42. B. Charlesworth, M. Nordborg, D. Charlesworth, *Genet. Res. Camb.* **70**, 155 (1997).
43. A. G. Young, T. Boyle, T. Brown, *Trends Ecol. Evol.* **11**, 413 (1996).
44. I. Olivieri, P. H. Gouyon, in *Metapopulation Biology*, I. A. Hanski, M. E. Gilpin, Eds. (Academic Press, San Diego, CA, 1997), pp. 293–324.
45. P. D. N. Hebert, M. J. Beaton, *Methodologies for Allozyme Analysis Using Cellulose Acetate Electrophoresis* (Helena Laboratories, Beaumont, TX, ed. 2, 1993).
46. H. W. Deng, M. Lynch, *Genetics* **147**, 147 (1997).

47. We thank T. Kawecki, M. Ackermann, D. Meyer, and S. Zweizig for critical comments to earlier version of the manuscript. This work was supported by the Swiss Science Foundation and NSF grant DEB-9973221

29 October 2001; accepted 26 November 2001

Systems Analysis of Ran Transport

Alicia E. Smith,[1] Boris M. Slepchenko,[2] James C. Schaff,[2] Leslie M. Loew,[2] Ian G. Macara[1]*

The separate components of nucleocytoplasmic transport have been well characterized, including the key regulatory role of Ran, a guanine nucleotide triphosphatase. However, the overall system behavior in intact cells is difficult to analyze because the dynamics of these components are interdependent. We used a combined experimental and computational approach to study Ran transport in vivo. The resulting model provides the first quantitative picture of Ran flux between the nuclear and cytoplasmic compartments in eukaryotic cells. The model predicts that the Ran exchange factor RCC1, and not the flux capacity of the nuclear pore complex (NPC), is the crucial regulator of steady-state flux across the NPC. Moreover, it provides the first estimate of the total in vivo flux (520 molecules per NPC per second and predicts that the transport system is robust.

In vitro studies of nucleocytoplasmic transport estimate a maximum rate of $\sim 10^3$ translocation events $NPC^{-1}\ s^{-1}$ (*1*). In the intact cell, however, steady-state flux rates might be a fraction of this value. To determine what factors contribute most toward the overall regulation of flux, we needed to integrate at a systems level the data for all the independent transport steps. This process required computational analysis. Cargo is shuttled through the NPC as a cargo-carrier complex, and a lower limit for cargo flux can be approximated if the steady-state flux of Ran is known, because at least one molecule of Ran is translocated in each direction for each complete cycle of carrier and cargo transport. We therefore used experimental and computational methods to estimate the steady-state flux rate for Ran in intact cells and to identify factors that most contribute to the global regulation of Ran transport.

We constructed a mathematical model of the Ran transport system in a mammalian cell using a modeling program called Virtual Cell (*2*, *3*). Biochemical reactions were localized in two subcellular compartments (cytosol and the nucleus), and flux rates between the compartments were calculated as the product of a permeability constant and the concentration difference across the nuclear envelope, describing facilitated diffusion by the transport carriers. Passive diffusion of Ran through the NPC was also incorporated. For the Ran transport cycle, reported data constrained the parameter values of reversible binding interactions and enzyme-mediated reactions (*4*–*10*) [Web table 1 and Web fig. 1 (*11*)]. All simulation results were obtained with the same parameter set, except where explicitly indicated.

For visualization of Ran import into the intact cell, the recombinant protein was modified with a fluorescent maleimide and was determined by several criteria to be functional [Web fig. 2 (*11*)]. This tagged Ran species (FL-Ran) in the model allowed direct comparisons of the simulation and experimental results. FL-Ran was injected into the cytosol of BHK-21 cells and imaged (at 0.5-s intervals) until nuclear accumulation reached a steady state (Fig. 1A) (*12*). Nuclear fluorescence intensities were converted to units of concentration by comparison to known standards (*12*). Import occurred with single exponential kinetics and reached a steady state within 12 to 30 s (at 23°C) (Fig. 1B) [Web fig. 3A (*11*)].

We also used a mutant species [Ran(T24N)], which is defective in binding to nuclear transport factor 2 (NTF2), the Ran

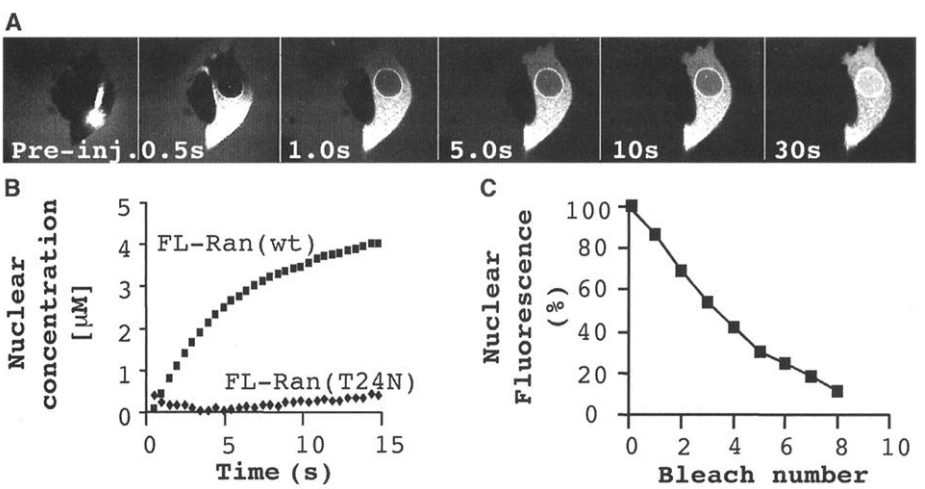

Fig. 1. Nucleocytoplasmic transport of FL-Ran in vivo. (**A**) Nuclear accumulation of FL-Ran in BHK-21 cells after cytosolic injection. (**B**) Comparison of time courses of nuclear accumulation for wild-type FL-Ran (initial cytosolic concentration = 7.8 μM) and T24N (initial cytosolic concentration = 9.0 μM). (**C**) Fluorescence loss in photobleaching on FL-Ran at steady state in microinjected BHK-21 cells. Graph shows remaining nuclear fluorescence intensity after each photobleaching cycle.

[1]Center for Cell Signaling, Departments of Pharmacology and Microbiology, University of Virginia, Charlottesville, VA 22908, USA. [2]Center for Biomedical Imaging Technology, University of Connecticut Health Center, Farmington, CT 06030, USA.

*To whom correspondence should be addressed. E-mail: igm9c@virginia.edu

import carrier (*4*, *13*, *14*). The rate of nuclear accumulation of FL-Ran(T24N) was <4% that of wild-type FL-Ran (Fig. 1B) and was similar to the rate of diffusion of green fluorescent protein (GFP) into the nucleus (*15*, *16*). Therefore, passive diffusion makes little contribution to the net flux of Ran through the NPCs of the intact cell.

To test whether all Ran molecules shuttle, we quantified the decrease in nuclear fluorescence intensity of FL-Ran at steady state after photobleaching part of the cytosol (*11*, *17*). Repeated bleaching of the cytosol caused almost complete loss of fluorescence in the nuclear compartment, indicating that most nuclear Ran shuttles (Fig. 1C) [Web fig. 3B (*11*)].

Virtual Cell can use three-dimensional (3D) geometry from an experimental image in spatial simulations (*2*). In our 3D simulations (*18*), microinjection is modeled as a brief (0.4 s), localized increase of the cytosolic FL-Ran concentration. The 3D simulation results resemble the experimental FL-Ran nuclear import and diffusion through the cytosol (Fig. 2A). A steep Ran guanosine triphosphate (GTP) gradient across the nuclear-cytoplasmic boundary is generated in the simulation, where 99.9% of free RanGTP is nuclear (Fig. 2B). Furthermore, the model predicts that a cytosolic concentration gradient of RanGTP complexed to carrier and to Ran-binding protein 1 (RanBP1) is established at steady state (Fig. 2B).

Whereas the spatial approximation is computationally intensive (taking ~4.5 hours of CPU time per simulation), in compartmental approximations, spatial diffusional gradients are not calculated (*19*), reducing computation time to 1 s of CPU time per simulation. Results obtained by both methods were similar, indicating that spatial diffusional gradients do not substantially affect Ran transport.

Using compartmental approximations, the initial rates of FL-Ran import were calculated from time courses for simulated cytosolic microinjections, and the initial conditions of all other variables represented steady-state values. The simulated maximum import rate (V_{max}) of 120 molecules NPC^{-1} s^{-1} closely matched the experimental V_{max}, which saturated at ~120 molecules NPC^{-1} s^{-1} (at 23°C), assuming 3000 pores per nuclear envelope (*20*), with a concentration at $\frac{1}{2}V$max ($K_{1/2}$) of ~2.0 μM (Fig. 2C). Moreover, model results were equivalent when a diffusive leak across the nuclear-cytoplasmic boundary of free Ran and FL-Ran was included (for FL-Ran <20 μM) (*16*).

In the model, release of 1 μM FL-Ran into the cytosol caused small sustained decreases in the concentrations of the carrier:RanGTP complex, and it caused transient decreases of NTF2:Ran guanosine diphosphate (GDP) and RanGDP (Fig. 3A). In contrast, nuclear concentrations of RanGTP, carrier, and NTF2 remained virtually unchanged (Fig. 3A). These observations highlight the robust quality of the model, because the Ran gradient across the nuclear-cytoplasmic boundary is buffered in response to perturbations.

We studied sensitivity of Ran flux to the model parameters by varying them over a wide range, one by one, while holding others at their nominal values. The Ran exchange factor RCC1 was most responsible for controlling steady-state flux rates in the system, whereas changes in the concentration of NTF2 or the permeability constant of NTF2:RanGDP had less effect (Fig. 3B, left panel). Other parameters—RanBP1, carrier concentrations, the permeability constant of carrier:RanGTP, and RanGAP (RanGTPase activating protein) (Fig. 3B, right panel)—had an effect only when their values were reduced by >90%. Thus, changes in RCC1 activity in vivo are predicted to have a predominant effect on steady-state Ran flux through the NPC.

To examine the effects of transport factors on the initial rate of Ran import, we increased the cellular concentrations of NTF2, RanBP1, or RanGAP or decreased the cellular concentrations of RCC1, both experimentally and within the mathematical model. This helped us to evaluate the underlying hypothesis that

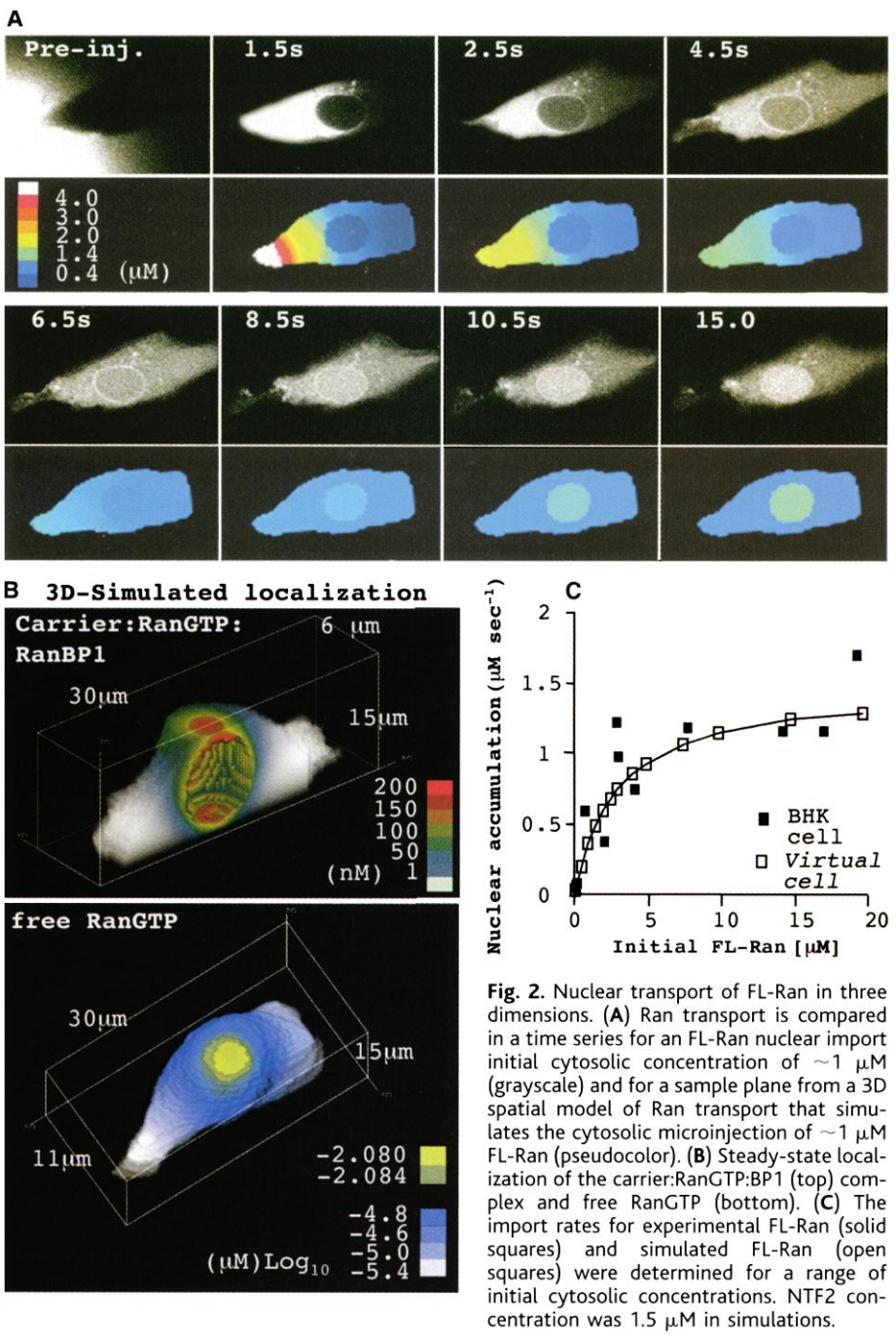

Fig. 2. Nuclear transport of FL-Ran in three dimensions. (**A**) Ran transport is compared in a time series for an FL-Ran nuclear import initial cytosolic concentration of ~1 μM (grayscale) and for a sample plane from a 3D spatial model of Ran transport that simulates the cytosolic microinjection of ~1 μM FL-Ran (pseudocolor). (**B**) Steady-state localization of the carrier:RanGTP:BP1 (top) complex and free RanGTP (bottom). (**C**) The import rates for experimental FL-Ran (solid squares) and simulated FL-Ran (open squares) were determined for a range of initial cytosolic concentrations. NTF2 concentration was 1.5 μM in simulations.

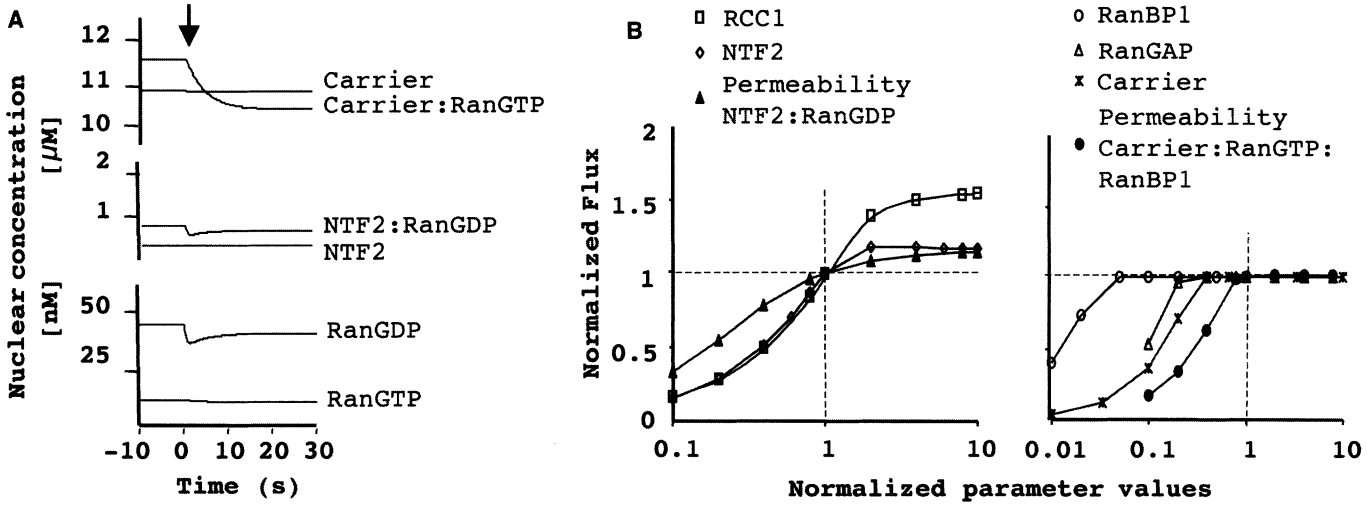

Fig. 3. Analysis of compartmental model for Ran transport. (**A**) Transients for simulated endogenous nuclear species concentrations were followed over time during recovery from the addition of 1 μM FL-Ran to the cytosolic compartment. (**B**) Global steady-state sensitivity analysis. Steady-state flux across the nucleocytoplasmic boundary was measured as individual parameters were changed independently over a 2 to 3 log scale. Normalized results are graphed such that (1, 1) indicates the nominal parameter set.

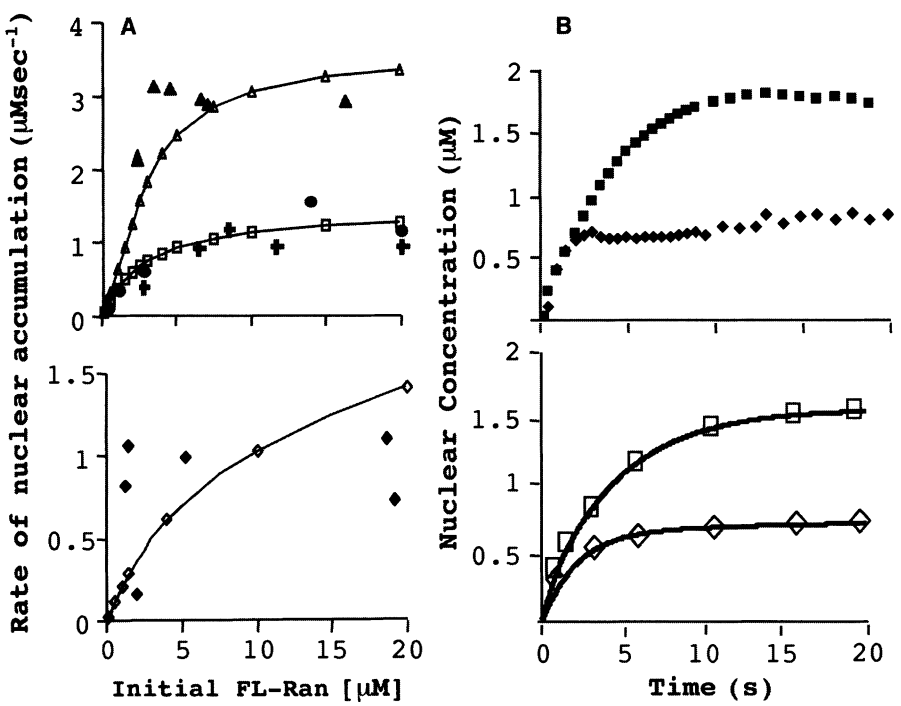

Fig. 4. Saturable and NTF2-dependent import rates of FL-Ran in vivo and in silico. (**A**) Top panel, experimental FL-Ran import in BHK-21 cells preinjected with NTF2 (solid triangles, 3.5 μM), RanBP1 (plus signs, 3.0 μM), or RanGAP (solid circles, 0.5 μM) was compared to simulated FL-Ran import with wild type (open squares) or increased amounts of NTF2 (open triangles, 4.0 μM). Lower panel, FL-Ran import rates were measured in temperature-shifted tsBN2 cells (solid diamonds) and compared with simulations with reduced RCC1 (open diamonds, 0.004 μM). (**B**) Time courses (upper panel) for nuclear accumulation of 1.2 μM FL-Ran in a temperature-shifted tsBN2 cell (solid diamonds) and BHK-21 cell (solid squares) was compared to a time course (lower panel) of simulated microinjection of 1.2 μM FL-Ran in shifted tsBN2 cell (open diamonds) and wild-type cell (open squares).

dictates how the molecules in our system are related and to test the predictive power of our model.

BHK-21 cells were preinjected with NTF2 (*21*) and the injection-marker GFP. After incubation (at 37°C for 1 hour) to allow recovery and establish steady state, FL-Ran was injected into the cytosol of the GFP-marked cells, and initial rates of import and steady-state distribution of FL-Ran were determined. Addition of exogenous NTF2 increased the steady-state nuclear-cytoplasmic ratio (N/C) for FL-Ran from ~4.0 to ~6.0 [Web fig. 4 and Web table 2 (*11*)], and the initial import rate saturated at a higher V_{max}, as predicted by the model (366 molecules NPC^{-1} s^{-1}) (Fig. 4A, top) [Web table 3 (*11*)]. Thus, in BHK-21 cells, the initial rate of FL-Ran import is limited by NTF2 availability and not by the flux capacity of the NPC. As further predicted by the model, the initial rate of Ran import in vivo was unaffected by increases in the levels of RanBP1 (*22*) or RanGAP (Fig. 4A, top).

When the concentration of RCC1 in the model was reduced by 99%, both the N/C ratio and the steady-state flux were reduced [Web tables 2 and 3 (*11*)]. However, this decrease in concentration of RCC1 caused only a small decrease in the initial rate of FL-Ran import in the model (Fig. 4). Experimentally, endogenous RCC1 can be reduced by warming tsBN2 cells (to 39.5°C), which contain a temperature-sensitive RCC1 allele (*23*, *24*). We measured FL-Ran import in temperature-shifted (at 39.5°C for 4 hours) tsBN2 cells with a preinjected mixture of Ran(T24N) and RanGAP, which further reduced the amount of nuclear RanGTP (Fig. 4B, top) (*23*, *25*). Although net nuclear accumulation was severely compromised under these conditions (Fig. 4B) [Web fig. 4 (*11*)], the initial rate of import was not altered (Fig. 4A). Thus, the simulation supports the finding that RCC1 depletion has only a weak effect on the initial rate of Ran import.

Our data demonstrate the value of the computational approach in understanding the global regulation of a compartmental transport process. The model provides an estimate for the steady-state, bidirectional flux of endogenous Ran in the intact cell, of 260 molecules NPC^{-1} s^{-1} [Web table 3 (*11*)]. Be-

cause one NTF2 and one carrier must translocate through the NPC for each Ran cycle, the estimated minimal value for traffic through the pore is ~520 molecules NPC^{-1} s^{-1} (at 23°C).

Several predictions result from the model: (i) Ran transport is robust, suggesting that fluctuations in concentrations of transport factors can be tolerated without catastrophic cellular effects. (ii) Modulation of RCC1 activity may be a relevant mechanism for the regulation of flux in vivo. (iii) Our calculated flux rate is lower than the measured maximum transport rate in vitro (*1*), suggesting that NPC permeability is not rate-limiting within intact cells. (iv) Simulations indicate that the free RanGTP concentration is orders of magnitude lower than the dissociation constant for Ran binding to several importins (*26*). This suggests that our understanding of import complex disassembly is incomplete and that additional factors may be essential in vivo for cargo unloading from certain importins (*27*). (v) The model confirms that a steep RanGTP gradient exists across the NPC (the free RanGTP N/C ratio is ~500). (vi) The spatial simulations predict that steady-state cytosolic gradients also exist, likely maintained by RanGAP activity toward the RanGTP exiting the nucleus. We speculate that such gradients could provide positional information on the location of the nucleus in the cell.

References and Notes

1. K. Ribbeck, D. Gorlich, *EMBO J.* **20**, 1320 (2001).
2. J. C. Schaff, B. M. Slepchenko, L. M. Loew, *Methods Enzymol.* **321**, 1 (2000).
3. The molecular species dynamics in the model are described by a set of partial-differential equations (reaction-diffusion type), $\partial[X]/\partial t = D_X\nabla^2[X] + \Sigma\nu$, where [X] is the concentration of species X, D_X is its diffusion coefficient, and the second term is the sum of the rates ν of the reactions affecting species X. The reversible reactions of the type $X + A \leftrightarrow AX$ [Web fig. 1 (11)] are described by mass action kinetics, $\nu = -k_{on}[X][A] + k_{off}[AX]$, where ν is the velocity, k_{on} is the forward reaction rate constant, and k_{off} is the reverse reaction rate constant. Enzyme-mediated reactions are approximated as irreversible, with Michaelis-Menten rates, $\nu = k_{cat}[E][X](K_m + [X])^{-1}$, where [E] is the enzyme concentration, k_{cat} is the catalytic-efficiency constant, and K_m is the Michaelis-Menten constant. Nuclear membrane flux densities are described: $j_X = P_X([X]_{cytosol} - [X]_{nucleus})$. Values of diffusion coefficients D_X; reaction parameters k_{on}, k_{off}, k_{cat}, and K_m; and permeabilities P_X are given in Web table 1 (*11*).
4. K. Ribbeck, G. Lipowsky, H. M. Kent, M. Stewart, D. Gorlich, *EMBO J.* **17**, 6587 (1998).
5. F. R. Bischoff, H. Ponstingl, *Proc. Natl. Acad. Sci. U.S.A.* **88**, 10830 (1991).
6. C. Klebe, H. Prinz, A. Wittinghofer, R. S. Goody, *Biochemistry* **34**, 12543 (1995).
7. C. Klebe, F. R. Bischoff, H. Ponstingl, A. Wittinghofer, *Biochemistry* **34**, 639 (1995).
8. K. M. Lounsbury, I. G. Macara, *J. Biol. Chem.* **272**, 551 (1997).
9. F. R. Bischoff, D. Gorlich, *FEBS Lett.* **419**, 249 (1997).
10. B. M. Paschal, L. Gerace, *J. Cell Biol.* **129**, 925 (1995).
11. Supplementary methods, tables, and figures are available on *Science* Online at www.sciencemag.org/cgi/content/full/295/5554/488/DC1.
12. C. Fink, F. Morgan, L. M. Loew, *Biophys. J.* **75**, 1648 (1998).
13. A. Smith, A. Brownawell, I. G. Macara, *Curr. Biol.* **8**, 1403 (1998).
14. P. R. Clarke, C. Klebe, A. Wittinghofer, E. Karsenti, *J. Cell Sci.* **108**, 1217 (1995).
15. M. Ormo *et al.*, *Science* **273**, 1392 (1996).
16. A. E. Smith, I. G. Macara, unpublished data.
17. K. J. Zaal *et al.*, *Cell* **99**, 589 (1999).
18. Compartmental and spatial simulations were run within Virtual Cell (*2*). For 3D simulations, a computational domain was decomposed into 100,860 orthogonal subvolumes (mesh size = 0.375 μm). Equations were approximated using the finite-volume approach. The resultant system of linear algebraic equations was solved with preconditioned conjugate gradients (time steps were 10 ms long). Reversible reactions were treated as infinitely fast (*2*).
19. Compartmental-approximation equations transform into $\partial[X]_i/\partial t = F_X \equiv \Sigma\nu + (-1)^i J_X$ with the "flux" rate $J_X = j_X S/V_i$, where the index i = 1, 2 denotes cytoplasm and nucleoplasm, respectively; S is the nuclear envelope surface area; and V_i is the volume of the ith compartment. We used in simulations $S/V_2 = 0.6\ \mu m^{-1}$ and $V_2/(V_1 + V_2) = 0.29$ (experimental average). Figures 2C and 4A show accumulation rates that were measured at 0.5 s.
20. V. C. Cordes, S. Reidenvach, W. W. R Franke, *Eur. J. Cell Biol.* **68**, 240 (1995).
21. W. D. Clarkson, H. M. Kent, M. Stewart, *J. Mol. Biol.* **263**, 517 (1996).
22. K. M. Lounsbury, S. A. Richards, K. L. Carey, I. G. Macara, *J. Biol. Chem.* **271**, 32834 (1996).
23. S. A. Richards, K. L. Carey, I. G. Macara, *Science* **276**, 1842 (1997).
24. H. Nishitani *et al.*, *EMBO J.* **10**, 1555 (1991).
25. E. Izaurralde, U. Kutay, C. Vonkobbe, I. W. Mattaj, D. Gorlich, *EMBO J.* **16**, 6535 (1997).
26. B. Senger *et al.*, *EMBO J.* **17**, 2196 (1998).
27. L. F. Pemberton, J. S. Rosenblum, G. Blobel, *J. Cell Biol.* **145**, 1407 (1999).

28. We thank the Macara laboratory, especially M. Lindsey, M. Nemergut, S. Plafker, K. Plafker, and A. Brownawell, and the Virtual Cell team and the Center for Biomedical Imaging Technology (University of Connecticut), especially A. Cowan, M. Terasaki, J. Carson, and J. Kirk. Supported by NIH grants GM-50526 (I.G.M.), NCRR-RR13186 (L.M.L.), and NIH-GM-20438 (A.E.S.).

25 July 2001; accepted 26 November 2001

Modulation of NMDA Receptor–Dependent Calcium Influx and Gene Expression Through EphB Receptors

Mari A. Takasu,* Matthew B. Dalva,* Richard E. Zigmond,† Michael E. Greenberg‡

Protein-protein interactions and calcium entry through the *N*-methyl-D-aspartate (NMDA)–type glutamate receptor regulate synaptic development and plasticity in the central nervous system. The EphB receptor tyrosine kinases are localized at excitatory synapses where they cluster and associate with NMDA receptors. We identified a mechanism whereby EphBs modulate NMDA receptor function. EphrinB2 activation of EphB in primary cortical neurons potentiates NMDA receptor–dependent influx of calcium. Treatment of cells with ephrinB2 led to NMDA receptor tyrosine phosphorylation through activation of the Src family of tyrosine kinases. These ephrinB2-dependent events result in enhanced NMDA receptor–dependent gene expression. Our findings indicate that ephrinB2 stimulation of EphB modulates the functional consequences of NMDA receptor activation and suggest a mechanism whereby activity-independent and activity-dependent signals converge to regulate the development and remodeling of synaptic connections.

During the development of the central nervous system, patterned neuronal activity drives the specification and maturation of synaptic connections (*1*, *2*). The NMDA-type excitatory glutamate receptor regulates these activity-dependent processes in part by controlling the entry of Ca^{2+} into neurons, which then activates signaling pathways that orchestrate neuronal development (*3*). Prior to the development of synapses, young neurons differentiate and begin the process of axon growth and guidance by a mechanism that is largely independent of neuronal activity (*4*). The molecular mechanisms that allow activity-dependent processes to build upon activity-independent cues are not clear.

The ephrins and their receptors, the Eph tyrosine kinases, are cell-surface proteins that play a role in mediating the initial interaction between axons and dendrites as well as other activity-independent processes during neural development (*5*, *6*). The Eph receptor proteins are classified into the EphA and EphB families on the basis of their preference for binding of glycosyl-phosphatidylinositol–linked ephrinA ligands or transmembrane ephrinB ligands, respectively. At the time of synaptogenesis, EphBs are localized to the